# Ultrahigh Photocatalytic Rate at a Single-Metal-Atom-Oxide

*Cong Wang, Ang Li, Chong Li, Shengbai Zhang,\* Hui Li, Xiaoyuan Zhou,\* Liming Hu,
Yibo Feng, Kaiwen Wang, Zhu Zhu, Ruiwen Shao, Yanhui Chen, Peng Gao,
Shengcheng Mao, Jun Huang, Ze Zhang, and Xiaodong Han\**

**Metal oxides, as one of the mostly abundant and widely utilized materials, are extensively investigated and applied in environmental remediation and protection, and in energy conversion and storage. Most of these diverse applications are the result of a large diversity of the electronic states of metal oxides. Noticeably, however, many metal oxides present obstacles for applications in catalysis, mainly due to the lack of efficient active sites with desired electronic states. Here, the fabrication of single-tungsten-atom-oxide (STAO) is demonstrated, in which the metal oxide's volume reaches its minimum as a unit cell. The catalytic mechanism in the STAO is determined by a new single-site physics mechanism, named as quasi-atom physics. The photogenerated electron transfer process is enabled by an electron in the spin-up channel excited from the highest occupied molecular orbital to the lowest unoccupied molecular orbital +1 state, which can only occur in STAO with $W^{5+}$. STAO results in a record-high and stable sunlight photocatalytic degradation rate of 0.24 $s^{-1}$, which exceeds the rates of available photocatalysts by two orders of magnitude. The fabrication of STAO and its unique quasi-atom photocatalytic mechanism lays new ground for achieving novel physical and chemical properties using single-metal-atom oxides (SMAO).**

As the most abundant substance on the earth, metal oxides have been extensively investigated and applied in environmental remediation and protection, energy conversion and storage, etc.[1–7] Due to the various electronic states, efforts and opportunities have been continuously made to create new structural units and functional activities of metal oxides for applications in catalysis. Pushing the size and dimension reduction of oxide to its limit, that is, the single metallic atom form of a metal oxide, can ultimately enhance the density of active catalytic sites.[8–10] More importantly, a rich tunability of oxygen coordination may fundamentally alter the catalytic mechanisms by creating new functionalized electronic states and active sites. For example, the catalytic behavior will transit from the properties of a solid to those of a single-metal-atom-oxide (SMAO), namely, those of a metallic atom and its coordinated oxygen atoms.

Dr. C. Wang, Dr. A. Li, H. Li, Y. Feng, K. Wang, Z. Zhu, Dr. Y. Chen,
Prof. S. Mao, Prof. J. Huang, Prof. X. Han
Institute of Microstructure and Property of Advanced Materials
Beijing Key Lab of Microstructure and Property of Advanced Materials
Beijing University of Technology
Beijing 100124, China
E-mail: xdhan@bjut.edu.cn

Dr. C. Li
International Laboratory for Quantum Functional Materials of Henan
School of Physics and Engineering
Zhengzhou University
Zhengzhou 450001, China

Prof. S. Zhang
Department of Physics
Applied Physics and Astronomy
Rensselaer Polytechnic Institute
Troy, NY 12180, USA
E-mail: zhangs9@rpi.edu

Prof. X. Zhou
College of Physics
Institute of Advanced Interdisciplinary Studies
Chongqing University
Chongqing 401331, China
E-mail: xiaoyuan2013@cqu.edu.cn

Prof. L. Hu
Department of Biological and Chemical Engineering
Beijing University of Technology
Beijing 100124, China

Dr. R. Shao, Prof. P. Gao
Electron Microscopy Laboratory
International Center for Quantum Materials
School of Physics
Peking University
Beijing 100871, China

Prof. J. Huang
School of Chemical and Biomolecular Engineering
Sydney Nano Institute
The University of Sydney Nano Institute
Sydney, New South Wales 2006, Australia

Prof. Z. Zhang
Department of Material Science
Zhejiang University
Hangzhou 310008, China

**ADVANCED
SCIENCE NEWS**

www.advancedsciencenews.com

**ADVANCED
MATERIALS**

www.advmat.de

Single-site catalysts have been widely investigated to enhance catalytic efficiencies and explore new activities.[10–12] Benefiting from the single-site strategy, the structure of the heterogeneous site can be rationalized to possibly reach an atomic-scale understanding.[12–15] It is then feasible to understand the structure–activity relationship and to develop predictable heterogeneous catalysis, that is, the single metallic atom form,[9,13] atomic clusters,[14–17] and sites with coordinated spheres[18–21] via distinctive anchoring routes and substrates. Excitingly, various single metallic atom catalysts[22–29] have been developed to realize numerous reactive sites with new mechanisms.

However, more strategies of single-sites and novel physical–chemical mechanisms are necessary to be explored. Especially for metal oxide catalytic sites, new opportunities arise by constructing new oxygen coordination configurations with variable number of metal–oxygen bonds and flexible substrates. In this paper, we report on a highly stable single-tungsten-atom oxide (STAO) photocatalyst, which is uniformly and homogeneously dispersed in aqueous solution as a byproduct of our coordinated route, where poly(ethylene oxide), as a support, was specifically designed to heterogeneously anchor STAO. Moreover, the interaction between the coordinated anchoring support and tungsten atom would not only form single-metal-atom oxide with monodispersity but also affect the photoelectronic states of STAO. To illustrate the strategy of STAO with respect to the traditional semiconductor catalyst and single-site catalyst of single metallic atoms on substrates, **Figure 1**a shows an example of conventional photocatalytic oxide: single crystal tungsten oxide and its electronic state of conduction and valence bands. Figure 1b illustrates that STAO exhibits a tungsten HOMO state near Fermi level. The intra-atomic d-orbitals allow an electron transition in the photoexcited STAO. Figure 1d shows a single Pt atom on the $TiO_2$ oxide which is derived from the pure Pt metals of Figure 1c. Comparing to Figure 1a,c,d, STAO in Figure 1b introduces a new single-site physics mechanism in which the spin-up and spin-down electrons in d-orbitals can

transit within the oxidized single tungsten atom, which is fundamentally different from the inter-d band electron transfer in single metallic atom materials (Figure 1d) and the interatomic $O_{2p}$–$W_{5d}$ electron transfer in conventional $WO_3$ crystal (Figure 1a). As expected, the excited states of intra-d-orbital electrons from the quasi-atom mechanisms combining with the maximized density of active sites from STAO can yield an ultra-high catalytic rate under illumination.

Our synthesized STAO is shown in **Figure 2**a, in which the monodispersed nature was characterized by scanning transmission electron microscopy (STEM). The single tungsten atoms can be observed as bright spots in the high-angle annular dark-field (HAADF) images (Figure 2b). X-ray photoelectron spectroscopy (XPS) and electron energy loss spectroscopy (EELS) are employed to reveal the chemical states of tungsten and oxygen, respectively (Figure 2c,d). Different from the spectrum of pure $W^{6+}$ (Figure S1, Supporting Information), the spectrum obtained from STAOs can be divided into two doublets. The main peaks are the $W^{6+}$ doublet at 35.8 eV ($W_{4f}7/2$) and 37.8 eV ($W_{4f}5/2$), while the $W^{5+}$ doublet appears as shoulders at 34.7 eV ($W_{4f}7/2$) and 36.7 eV ($W_{4f}5/2$).[30] The chemical state of oxygen is examined by EELS as presented in Figure 2d. As a comparison, the spectrum from a commercially available $WO_3$ particle as a reference sample is shown as the black solid line. Compared with the EELS spectrum of the $WO_3$ particle reference, the STAO spectrum shows that P1, P2, and P4 diminish. The disappearance of the P1 and P2 may be attributed to the fact that in $WO_3$ particles, the number of empty states $O_{2p}$ is determined by the occupancy of the conduction band, and by the degree of the metal–oxygen bond covalency,[31] which largely decreases in STAOs. On the other hand, the disappearance of P4, which is a characteristic of the second-nearest-neighbor W—O—W peak,[32] is consistent with monodispersing STAO without nearest-neighboring W atoms. To further confirm the coordination configuration of STAO, extended X-ray absorption fine structure (EXAFS)
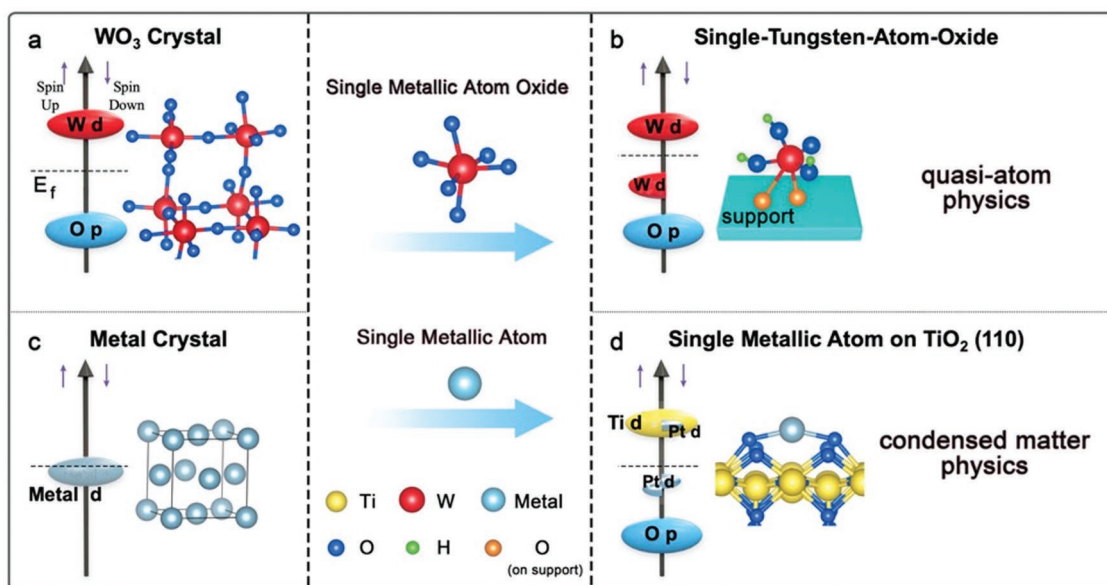


**Figure 1.** a–d) Electronic properties and its structure of a $WO_3$ crystal, a single tungsten atom oxide, a noble metal crystal, and a single Pt atom on $TiO_2$ (110). The electronic property of STAO is distinct, compared with those of the metal oxide crystal and single metallic atom on support.
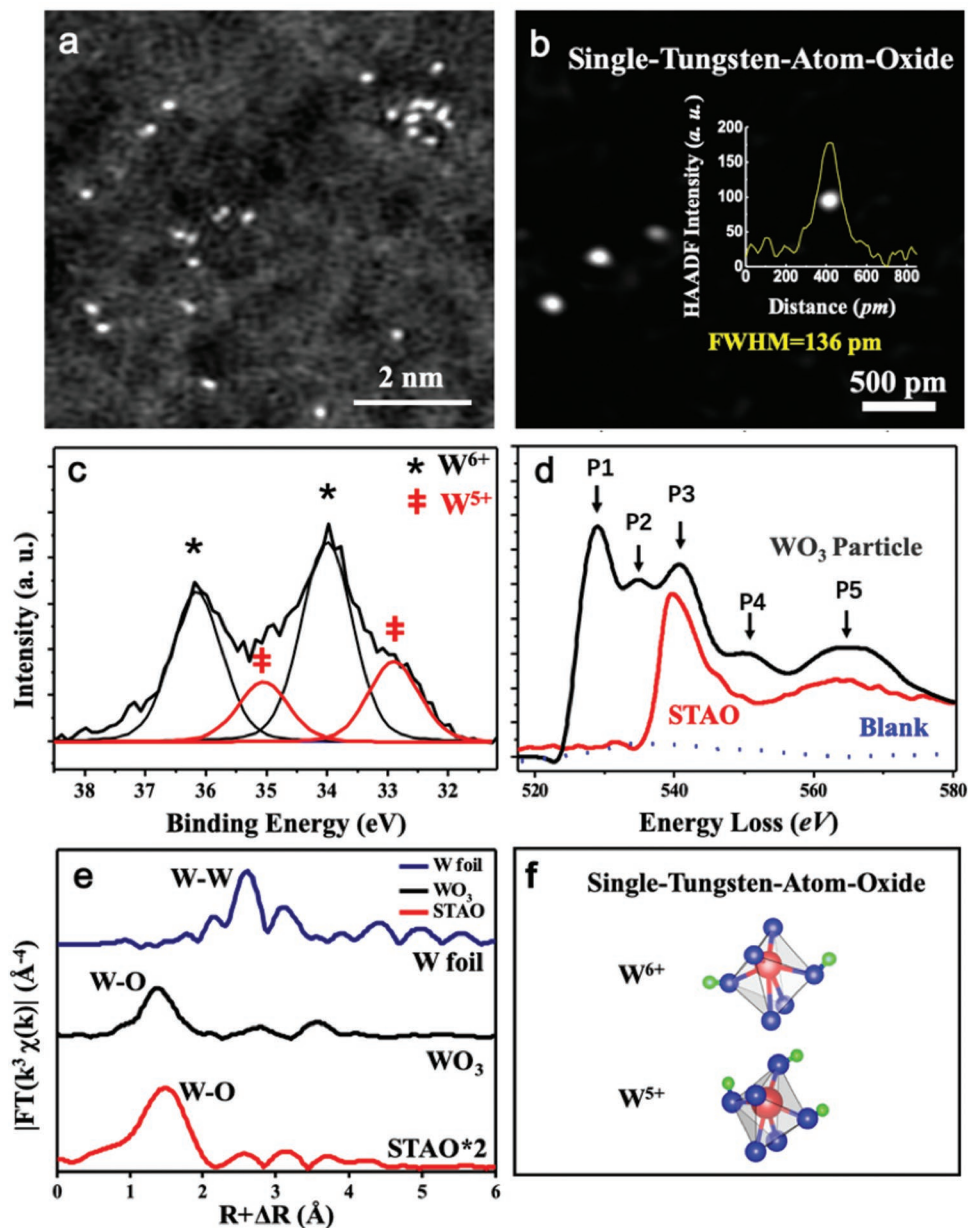
**ADVANCED
SCIENCE NEWS**

www.advancedsciencenews.com

**ADVANCED
MATERIALS**

www.advmat.de

**Figure 2.** Characterizations and chemical analysis of STAO. a) A $C_s$-corrected STEM-HAADF image shows monodispersed single tungsten atoms. b) A $C_s$-corrected STEM-HAADF image at a larger magnification. Inset shows the brightness of the full width at half maximum (FWHM), which is consistent with the diameter of a tungsten atom. c) XPS indicates that tungsten in STAOs has two valence states of 5+ and 6+. The black line is $W^{6+}$ and the red line is $W^{5+}$. d) EELS data of O K-edge of STAOs (red line). For comparison, those of $WO_3$ particles (black line) and blank (blue line) are also shown. e) The $K_2$-weighted Fourier transform spectra of STAO, W foil, and $WO_3$ were used as reference samples. f) Coordination of STAO with 6+ and 5+.

investigation was carried out and the detail structural information about STAO is shown in Figure 2e. In comparison, the EXAFS spectrum of W foil and $WO_3$ is shown in the same figure. The W-foil spectrum in Figure 2e shows a main peak at 2.6 Å, corresponding to the W—W coordination of W foil. In comparison, no peak at the position of 2.6 Å of the STAO spectrum indicates that there is no W cluster in STAO. Further, the single peak in STAO located at 1.5 Å can be assigned to W—O nearest neighbor coordination which is similar to that of $WO_3$ at 1.31 Å and suggests an octahedron coordination. The longer W—O bonding length of 1.5 Å in STAO indicates

the W—O octahedron is distorted and possesses unsaturated bonding features derived from single-tungsten-atom oxide. The EXAFS results are consistent with the evidence of the single W atoms revealed directly from TEM HAADF observation shown in Figure 2a,b, and also consistent with the XPS and EELS analysis (Figure 2c,d). Combining all above information together, the $W-O_6$ coordination, STAO with $W^{6+}$ and $W^{5+}$ are constructed by distorted octahedron structural models and are schematically presented in Figure 2f. Based on these information, the coordination of STAO with PEO is suggested to share two oxygen atoms with an edge of the W—O octahedron as
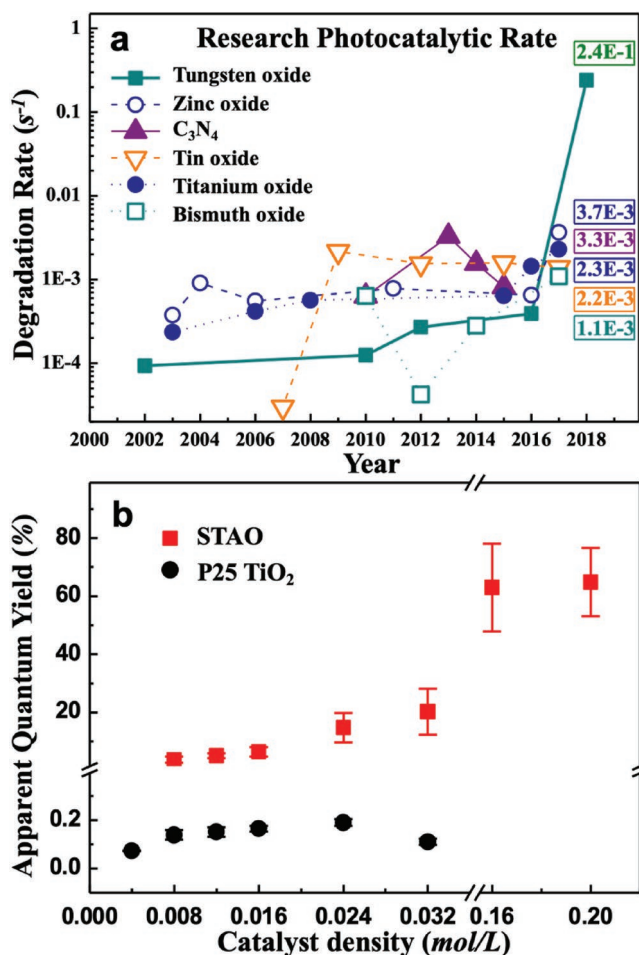
**ADVANCED
SCIENCE NEWS**

www.advancedsciencenews.com

**ADVANCED
MATERIALS**

www.advmat.de

**Figure 3.** Photocatalytic degradation performance of STAO. a) Photocatalytic rate of dye by available catalysts under sunlight (AM1.5G). b) AQY as a function of catalyst density. Note that AQYs of P25s are at least 100 times smaller than those of STAOs. Error bars represent standard deviation given by at least three independent measurements.

efficiency at a low saturation density (Figure S5, Supporting Information), while STAO's efficiency increases linearly as its density increases. When it comes to 0.2 mol L$^{-1}$, an AQY of STAO of ≈64.82% is achieved, and external quantum efficiency is shown in Figure S6 (Supporting Information). The kinetics of dye adsorption in the dark performed for different dye initial concentration is shown in Figure S4 (Supporting Information). It can be seen as Langmuirian equilibrium adsorption after 1–2 h. Then, the optimized turnover frequency is calculated as $6.13 \times 10^{-4}$ s$^{-1}$, where an equilibrated adsorption is reached under sufficient dye to steady-state concentration. To verify the stability and robustness of the catalyst, first to fifth photocatalytic degradation (see Method, Supporting Information) results of STAO showed no significant decrease in efficiency (Figure S7, Supporting Information). Furthermore, the high-resolution TEM images of the durable photocatalyst indicate that the SMAO has been kept as monodispersity after five times repeated degradation performances (Figure S8a, Supporting Information). Figure S8b,c (Supporting Information) shows that the photocatalyst with five times recycle run has no observable change in chemical valence state and the radical signal in electron spin resonance (ESR). Additionally, the photocatalysts are also robust on various supports (Tween, PEO-PPO-PEO, and TiO$_2$), and all of them exhibit high and stable photocatalytic efficiencies (Figure S9a–c, Supporting Information). Figure S9d–f (Supporting Information) shows that the monodispersed metal oxides on the supports are intact after the recycling. The ESR and XPS data in Figure S9g,h (Supporting Information) further indicate that the physical properties of the STAOs on other supports have not changed either.

Our experiments raise three fundamental questions: (1) the microscopic origin of W$^{5+}$ in relation to the coordinated anchoring of STAOs on poly(ethylene oxide), (2) the physical nature of HOMO–LUMO states of STAO in relation to the oxidation states of tungsten, and (3) the electron transfer mechanism of W$^{5+}$ in the STAO limit.

The large amount of STAOs in our experiments suggests that their formation via a coordination route with poly(ethylene oxide) is energetically favored. STAOs can vary in their tungsten valency between 5+ and 6+ by a different hydrogen attachment, for example, W$^{5+}$ in WO$_4$H$_3$ and W$^{6+}$ in WO$_4$H$_2$. Based on the coordination models of STAO in Figure 2, the first-principles total-energy calculations for the coordination were conducted and suggest that the formation energy (Table S2, Supporting Information) for W$^{6+}$ is −0.68 eV, whereas that for W$^{5+}$ is −0.69 eV. Both configurations prefer the distorted octahedron geometry as a result of strong binding between STAOs and poly(ethylene oxide), as well as other supports. In our experiment, the STAO–poly(ethylene oxide) complexes were often present in a solution, which facilitated the conversion between W$^{5+}$ and W$^{6+}$. This process is demonstrated in **Figure 4**a where a W$^{6+}$ complex reacts with one hydroxyl to form a W$^{5+}$ complex plus 1/2 H$_2$O$_2$ through proton-coupled electron transfer. We have performed ESR measurements in the dark (Figure S10a–c, Supporting Information), which confirmed the presence of dimethyl pyridine N-oxide-OH radicals. This is a direct evidence that H$_2$O$_2$ is present in W$^{5+}$ complex. On the other hand, Figures S11 and S12 and Table S2 (Supporting Information) show that the catalytic efficiency increases considerably when

shown in Figure 4a,b. The detailed theoretical consideration and calculation is shown in the Supporting Information and Figure S5 (Supporting Information).

The STAO exhibits superior catalytic performances in the photocatalytic degradation of dyes (methyl orange, methyl red, and dimethyl yellow, shown in Figure S2, Supporting Information). The photocatalytic rate under simulated sunlight (98.5 mW cm$^{-2}$, detailed characterization in Method, Supporting Information) of 0.24 s$^{-1}$ exceeds those of available photocatalysts by two orders of magnitude, as summarized in **Figure 3**a and Table S1 (Supporting Information). The performance of STAO can be directly visualized in Figure S3, Movies S1 and S2 (Supporting Information). It is demonstrated in Figure 3b that the 365 nm apparent quantum yield (AQY, 1.84 mW cm$^{-2}$) of STAO is also at least two orders of magnitude larger than that of commercial TiO$_2$ nanoparticles (P25) at the same density (detailed spectra are shown in Figure S4, Supporting Information). STAO has significantly less light scattering, and the interactions among STAOs are much weaker than those among nanoparticles when the density of the catalyst comes to a saturation. Consequently, P25 tends to reach its maximum

**ADVANCED
SCIENCE NEWS**
www.advancedsciencenews.com

**ADVANCED
MATERIALS**
www.advmat.de

the pH decreases from ≈7 to 1, which signals an increase in the concentration of the $W^{5+}$ complexes.

In light of the different hydrogen coordination types, one can expect noticeable changes in the absorption spectrum. Our calculation yields a gap of 4.96 and 3.03 eV for $W^{6+}$ and $W^{5+}$ (Figure 4b), respectively, which matches the measured absorption peaks at 5.11 and 3.02 eV (Figure S13, Supporting Information). The marked difference in the HOMO-LUMO gaps between $W^{5+}$ and $W^{6+}$ suggests that one could determine the role of $W^{5+}$ and $W^{6+}$ in the dye degradation reaction by tuning the light wavelength. Photocatalytic degradation

experiments were carried out with a 230 nm (5.39 eV) laser to preferentially excite $W^{6+}$ and, separately, with a 380 nm (3.26 eV) laser to preferentially excite $W^{5+}$. A similarly excellent efficiency obtained at 380 nm light demonstrates that the STAO complexes with $W^{5+}$ play the dominant role in the reaction.

In order to understand why STAO complexes with $W^{5+}$ possess a high catalytic efficiency, we calculate the electronic orbitals for STAO complexes. The additional electron of $W^{5+}$ occupies a spin-up HOMO state in Figure 4b, which is empty in $W^{6+}$, and results in two important consequences: (a) $W^{5+}$ is spin-polarized with 1 μB. The presence of spin dictates
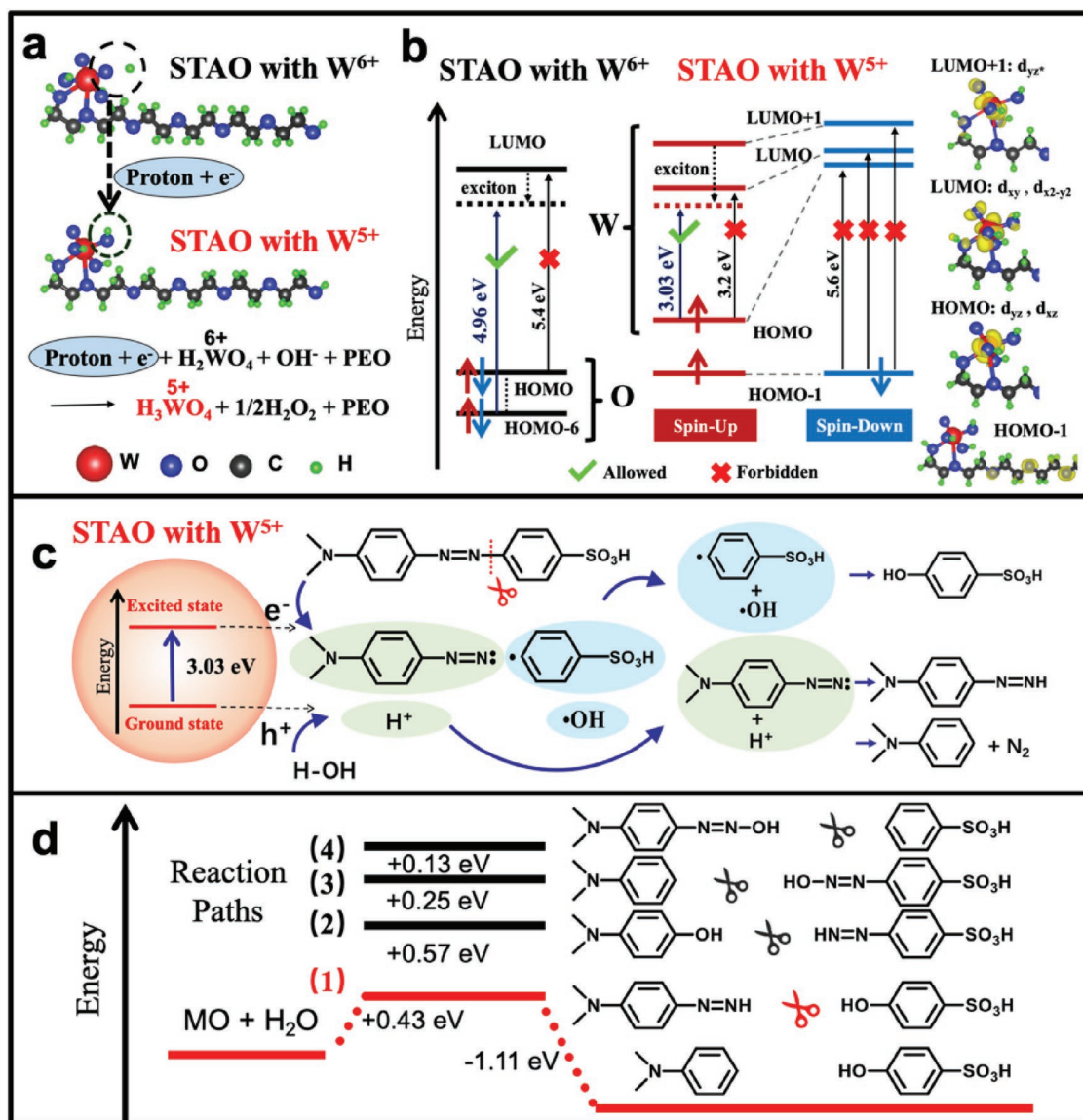


**Figure 4.** Mechanism of record-high catalytic rate in STAOs. a) Schematic illustration of $W^{5+}$ formation in STAO. Red, blue, black, and green balls are tungsten, oxygen, carbon, and hydrogen atoms, respectively. b) TD-DFT calculated the occupations and transitions between states in $W^{6+}$ (left panel) and separately in $W^{5+}$ (middle panel). Arrows ↑ and ↓ denote spins. Dashed lines connect spin-up and down channels in the same band. The HOMO, LUMO, and LUMO+1 bands for $W^{5+}$ have been decomposed (right panel) according to the tungsten atomic orbitals. c) Photocatalytic degradation reaction: upon photoexcitation, the hole dissociates an $H_2O$ into $H^+$ and ·OH. The electron cleaves a C−N bond in the azo-benzenesulfonic group. The resulting $H^+$ then reacts with 4-(2λ²-diazenyl)-N,N-dimethylaniline (green) to form N,N-dimethylaniline, while the ·OH reacts with benzenesulfonic acid radical (blue) to form p-hydroxy benzene sulfonic acid. d) Four possible cleavage pathways (1)–(4) with calculated activation energies. It shows that the $N_2$ release via a proton transfer reaction [i.e., path (1) marked in red] is energetically favored.

that the singly occupied HOMO states spin split. (b) The $W^{5+}$ HOMO state is a tungsten d-state, as opposed to the oxygen p-state of $W^{6+}$. Our analysis shows that the HOMO state of $W^{5+}$ is made of tungsten $d_{xz}$ and $d_{yz}$ orbitals, the LUMO state is made of tungsten $d_{xy}$ and $d_{x^2-y^2}$ orbitals, while the LUMO+1 state is made of a tungsten $d_{yz*}$ orbital (see yellow clouds in Figure 4b). While optical transitions between different spin channels are forbidden, within the same spin channel, most of the low-energy transitions are also forbidden due to local d-orbital symmetry of the wavefunctions, except for the transitions from HOMO to LUMO (very weak) and from HOMO to LUMO+1 (strong). Note that due to the strong localization of d orbitals in atomic-like STAOs, here one cannot neglect the excitonic effect when calculating optical transitions. As it turns out, the effect is large, for example, 4.53 eV for the HOMO to LUMO+1 transition to result in an optical gap of 3.03 eV. Similarly, when calculating the transition for the $W^{6+}$ states, the excitonic effect is also important and the minimum transition energy gap is 4.96 eV and is between HOMO–6 (an oxygen p-state) and LUMO. The HOMO–LUMO positions were further confirmed by ultraviolet photoelectron spectrum (UPS). Figure S14 (Supporting Information) shows the valence band maximum (3.3 eV referring to fermi level) of STAO. Since the bandgap of STAO is 3.02 eV based on absorption result, it can be calculated that the conduction band minimum is 0.28 eV. Figure S14 (Supporting Information) also demonstrates that the work function of STAO is 21.2 – 16.03 = 5.07 eV, which is consistent with previous reported values of tungsten oxide.[33] Thus, the LUMO and HOMO level can be calculated as −5.35 and −8.37 eV, respectively. Since the reduction potential of methyl orange was measured and calculated to be located at −5.4 eV around,[34] which is consistent with band structure measurement and simulated results. When optical excitation creates electron–hole pairs in STAO with $W^{5+}$ (Figure 4c), the photogenerated holes split H−OH to result in the formation of hydroxyl radicals. The photogenerated electrons, on the other hand, would cause a selective cleavage of the C−N bonds in the azo-benzenesulfonic group of the methyl orange molecules.[35,36] The resulting hydroxyl radicals and benzenesulfonic radicals combine to form p-hydroxybenzenesulfonic acid ($m/z$ = 172, high-performance liquid chromatography mass spectrometry (HPLC-MS), negative mode). Should this happen, $N,N$-dimethylaniline ($m/z$ = 122, HPLC-MS, positive mode) will also be present in the final products. The experimental results in Figures S15 and S16 (Supporting Information) show that both $N,N$-dimethylaniline and p-hydroxy benzenesulfonic acid are detected as the dominant reaction products. The above catalytic route is not only in full agreement with experiments but also supported by first-principles calculations. Figure 4d shows that, among the various possible cleavages (1)–(4), pathway (1) is energetically favored.

Single-site photocatalyst of Ti, V, Mo, and Cr oxide moieties on porous zeolite and silica substrates was developed[11,37,38] and high efficiency of catalytic effects was demonstrated.[10,39,40] To stabilize the single sites, a porous silica substrate is a prerequisite, more flexible, or new substrates are expected. The tetrahedron coordinated $Ti^{3+}$ and/or $Ti^{4+}$ models of the single sites were proposed based on EXAFS results, further evidence from microscopy to clarify the spatial distributions of these

single sites is necessary in the future to better understand the structure–activity relationships and design more efficient catalysts. Recently, with the significant progress of surface organometallic chemistry,[12,15,18] many single-site heterogeneous catalysts such as the monomeric, dimeric Cr silicates,[41] and aluminates[42] were designed and developed to elucidate the complicated structure–activity relationships of heterogeneous catalyst. While some of the complicated catalytic mechanisms, such as the Philips single-site catalysts are still uncertain,[43] continuous efforts along this trend are highly demanded. Following the single-site catalyst route, Pt single atomic catalyst claimed a new type in the family[22,23,26,28] and rapid progress was made along this way.[9,13] New valence states and activity sites of these single (or bi, tri, or multiple) metallic atoms coordinated with distinctive but well-defined oxide, sulfide, and halide configurations are highly expected in the future.

Indeed, single-site catalysts have broader expansions than absolute single-atom configurations and continuously have new family members. Once the functionalized structural units or molecules are identified and isolated and stabilized, the concepts of single-site catalysts apply. Significant progress along this trend is highly expected. As a single-site catalyst, STAO not only is synthesized by a novel flexible coordinated route but also provides a new electronic state and an octahedron single-site mechanism in photocatalytic physics. STAO with six-oxygen octahedron coordination can be viewed as a typical model of active sites to investigate such structure–activity relationship precisely. Note that the electronic state of single $W^{5+}$ species with octahedron oxygen and the proposed single-site mechanisms are distinctive from other immobilized metal oxide sites, for example, high-valent isolated tungsten oxide site in metathesis.[44,45] STAO exhibits flexible structure with efficient single metallic oxidized sites anchored on small polymer molecules enables it uniformly and homogeneously dispersed in aqueous solution but heterogeneously anchored on supports. This hybrid character of the homogeneously dispersed heterogeneous STAO enables an extremely high catalytic efficiency by two orders than those of the currently available ones. Finally, with aberration corrected TEM characterization, unambiguous evidence of the isolated single tungsten atoms together with the coordinated oxygen configurations were revealed clearly, which provides spatial distributed information of these isolated single atomic active sites directly and visually. Thus, STAO and its relevant researches would accelerate the investigation of single-site catalysts and give insights of the grounds of surface organometallic chemistry. The diversified oxygen coordination will bring hopes of creating new electronic states and providing opportunities to design novel heterogeneous catalytic activities with STAO's physical mechanism and strategy in combination with surface organometallic chemistry.

In summary, an ultrahigh catalytic rate of 0.24 $s^{-1}$ under sunlight and a 64.82% AQY at 365 nm are achieved with stability by STAO, which both exceed those of available photocatalysts by at least two orders of magnitude. The ultrahigh efficient photocatalytic degradation is mainly attributed to the high density of active catalytic sites and the novel quantum physics in STAO. The properties of the STAO critically depend on the coordination with oxygen, as well as different from bulk oxide for it replaces bulk band edge p–d transition by pseudo-atomic d–d transition. Equally important is the simple method to anchor

**ADVANCED
SCIENCE NEWS**

www.advancedsciencenews.com

**ADVANCED
MATERIALS**

www.advmat.de

coordinated single-metal-atom oxides on supports. The methodology for the anchoring of STAOs can be readily adopted for a wide range of transition metal oxides (such as Mo, Nb, and Zr, as shown in Figure S17, Supporting Information), and is anticipated to be effective for chalcogenides and halides with outstanding properties for catalysis, energy conversion, information storage, environmental protection, chiral optics, and quantum information science.

## Supporting Information

Supporting Information is available from the Wiley Online Library or from the author.

## Conflict of Interest

The authors declare no conflict of interest.

## Keywords

photocatalysis, single-metal-atom-oxides, single-site mechanism

[1] S. J. Tesh, T. B. Scott, *Adv. Mater.* **2014**, *26*, 6056.
[2] C.-C. Chen, W.-H. Ma, J.-C. Zhao, *Chem. Soc. Rev.* **2010**, *39*, 4206.
[3] H. Schmies, A. Bergmann, J. Drnec, G. Wang, D. Teschner, S. Kuhl, D. Sandbeck, S. Cherevko, M. Gocyla, M. Shviro, M. Heggen, V. Ramani, R. E. Dunin-Borkowski, K. Mayrhofer, P. Strasser, *Adv. Energy Mater.* **2017**, 1701663.
[4] X. Liu, J.-Q. Huang, Q. Zhang, L.-Q. Mai, *Adv. Mater.* **2017**, *29*, 1601759.
[5] P. Li, X.-Y. Chen, H.-C. He, X. Zhou, Y. Zhou, Z.-G. Zou, *Adv. Mater.* **2017**, 1703119.
[6] Z.-G. Zou, J.-H. Ye, K. Sayama, H. Arakawa, *Nature* **2001**, *414*, 625.
[7] J. H. Myung, D. Neagu, D. N. Miller, J. T. S. Irvine, *Nature* **2016**, *537*, 528.
[8] A. T. Bell, *Science* **2003**, *299*, 1688.
[9] A.-Q. Wang, J. Li, T. Zhang, *Nat. Rev. Chem.* **2018**, *2*, 65.
[10] H. Yamashita, K. Mori, *Chem. Lett.* **2007**, *36*, 348.

[11] J. M. Thomas, R. Raja, D. W. Lewis, *Angew. Chem., Int. Ed.* **2005**, *44*, 6456.
[12] J. D. Pelletier, J. M. Basset, *Acc. Chem. Res.* **2016**, *49*, 664.
[13] L.-C. Liu, A. Corma, *Chem. Rev.* **2018**, *118*, 4981.
[14] M. Anpo, J. M. Thomas, *Chem. Commun.* **2006**, *31*, 3273.
[15] C. Coperet, A. C. Vives, M. P. Conley, D. P. Estes, A. Fedorov, V. Mougel, H. Nagae, F. N. Zaurur, P. A. Zhizhko, *Chem. Rev.* **2016**, *116*, 323.
[16] G. G. Hatky, *Chem. Rev.* **2000**, *100*, 1347.
[17] H. Guesmi, R. Grybos, J. Handzlik, F. Tielens, *RSC Adv.* **2016**, *6*, 39424.
[18] C. Coperet, *Acc. Chem. Res.* **2019**, *52*, 1697.
[19] S. Kramer, N. R. Bennedsen, S. Kegnas, *ACS Catal.* **2018**, *8*, 6961.
[20] T. J. Marks, *Acc. Chem. Res.* **1992**, *25*, 57.
[21] E. Y. X. Chen, *Chem. Rev.* **2009**, *109*, 5157.
[22] J. H. Kwak, J.-Z. Hu, D.-H. Mei, C.-W. Yi, D. Kim, C. H. F. Peden, L. F. Allard, J. Szanyi, *Science* **2009**, *325*, 1670.
[23] B.-T. Qiao, A.-Q. Wang, X.-F. Yang, L. F. Allard, Z. Jiang, Y. Cui, J.-Y. Liu, J. Li, T. Zhang, *Nat. Chem.* **2011**, *3*, 634.
[24] M. Yang, S. Li, Y. Wang, J. A. Herron, Y. Xu, L. F. Allard, S. Lee, J. Huang, M. Mavrikakis, M. Flytzani-Stephanopoulos, *Science* **2014**, *346*, 1498.
[25] P.-X. Liu, Y. Zhao, R.-X. Qin, S.-G. Mo, G.-X. Chen, L. Gu, D. M. Chevrier, P. Zhang, Q. Guo, D. Zang, B. Wu, G. Fu, N.-F. Zheng, *Science* **2016**, *352*, 797.
[26] J. Jones, H.-F. Huang, A. T. DeLaRiva, E. J. Peterson, H. Pham, S. R. Challa, G. Qi, S. Oh, M. H. Wiebenga, X. Hernandez, Y. Wang, A. K. Datye, *Science* **2016**, *353*, 150.
[27] J.-J. Shan, M.-W. Li, L. F. Allard, S. Lee, M. Flytzani-Stephanopoulos, *Nature* **2017**, *551*, 605.
[28] Z. Zhang, Y. Zhu, H. Asakura, B. Zhang, J. Zhang, M. Zhou, Y. Han, T. Tanaka, A. Wang, N. Yan, *Nat. Commun.* **2017**, *8*, 16100.
[29] L. Wang, W. Zhang, S. Wang, Z. Gao, Z. Luo, X. Wang, R. Zeng, A. Li, H. Li, M. Wang, X. Zheng, J. Zhu, W. Zhang, C. Ma, R. Si, J. Zeng, *Nat. Commun.* **2016**, *7*, 141036.
[30] C. Wang, B. Zhou, X. Zeng, Y. Hong, Y. Gao, W. Wen, *J. Mater. Chem. C* **2015**, *3*, 177.
[31] F. M. F. De Groot, M. Grioni, J. C. Fuggle, J. Ghijsen, G. Sawatzky, H. Petersen, *Phys. Rev. B* **1989**, *40*, 5715.
[32] J. Purans, A. Kuzmin, P. Parent, C. Laffon, *Electrochim. Acta* **2001**, *46*, 1973.
[33] G. Halek, I. D. Baikie, H. Teterycz, P. Halek, P. S. Wozniak, K. Wisniewski. *Sens. Actuators, B* **2013**, *187*, 379.
[34] S. H. Li, Y. Zhao, J. Chu, W. Li, H. Q. Yu, G. Liu. *Electrochim. Acta* **2013**, *92*, 93.
[35] K. Li, L. Yan, Z. Zeng, S. Luo, X. Luo, X. Liu, H. Guo, Y. Guo, *Appl. Catal., B* **2014**, *156*, 141.
[36] H. H. Huo, X. Shen, C. Wang, L. Zhang, P. Rose, L. Chen, K. Harms, M. Marsch, E. Meggers, *Nature* **2014**, *515*, 100.
[37] H. Yamashita, K. Ikeue, T. Takewaki, M. Anpo, *Top. Catal.* **2002**, *18*, 95.
[38] H. Yamashita, H. Nakao, M. Okazaki, M. Anpo, *Stud. Surf. Sci. Catal.* **2003**, *146*, 795.
[39] J. Severn, J. Chadwick, R. Duchateau, N. Friederichs, *Chem. Rev.* **2005**, *105*, 4073.
[40] M. McDaniel, *Adv. Catal.* **2010**, *53*, 123.
[41] C. Brown, J. Krzystek, R. Achey, A. Lita, R. Fu, R. W. Meulenberg, M. Polinski, N. Peek, Y. Wang, L. J. van de Burgt, S. Profeta, A. E. Stiegman, S. L. Scott, *ACS Catal.* **2015**, *5*, 5574.
[42] J. Sattler, J. Ruiz-Martinez, E. Santillan-Jimenez, B. M. Weckhuysen, *Chem. Rev.* **2014**, *114*, 10613.
[43] E. Groppo, G. A. Martino, A. Piovano, C. Barzan, *ACS Catal.* **2018**, *8*, 10846.
[44] S. Lwin, Y. Li, A. I. Frenkel, I. E. Wachs, *ACS Catal.* **2016**, *6*, 3061.
[45] A. Chakrabarti, M. Gierada, J. Handzlik, I. E. Wachs, *Top. Catal.* **2016**, *59*, 725.